A disordered nanoparticle model for 6-line ferrihydrite

BENJAMIN GILBERT,[1,]* JASMINE J. ERBS,[2] R. LEE PENN,[2] VALERI PETKOV,[3] DINO SPAGNOLI,[4] AND
GLENN A. WAYCHUNAS[1]

[1]Earth Sciences Division, Lawrence Berkeley National Laboratory, MS 74R316C, 1 Cyclotron Road, Berkeley, California 94720, U.S.A.
[2]Department of Chemistry, University of Minnesota, 207 Pleasant Street S.E., Minneapolis, Minnesota 55455, U.S.A.
[3]Department of Physics, Central Michigan University, Mt. Pleasant, Michigan 48848, U.S.A.
[4]School of Chemistry and Biochemistry, University of Western Australia, Crawley, Western Australia 6009, Australia

ABSTRACT

Much of the bioavailable and geochemically reactive iron in aerobic, circumneutral settings is frequently found in the form of nanoscale particles of a hydrated iron(III) oxyhydroxide phase known as ferrihydrite. Developing useful structural descriptions of defective nanophases such as ferrihydrite has long posed significant challenges. Recently, Michel et al. (2007, 2010) proposed a structural model for ferrihydrite in place of the long-accepted model of Drits et al. (1993). Both models reproduce to high accuracy certain forms of X-ray scattering data from powdered ferrihydrite. However, discrepancies remain that we hypothesized are due to forms of structural disorder not easily represented by existing models. To test this hypothesis, we performed a novel structural analysis of total X-ray scattering data acquired from 6-line ferrihydrite. We generated three candidate whole-nanoparticle models of ferrihydrite composed of a two-phase *Drits* model, the *Michel* model, and a *hybrid* phase based on a single-phase *Drits* model that incorporated tetrahedral Fe sites, creating a lattice in which the *Michel* model was one of many possible topologies. We implemented a reverse Monte Carlo (RMC) approach to explore alternative configurations of iron occupancies plus structural disorder, and to refine the nanoparticle structure using both the reciprocal and real-space forms of the X-ray scattering data. We additionally used oxygen *K*-edge X-ray absorption spectroscopy to semi-quantitatively assess the ratio of protonated:non-protonated oxygen sites in an iron(III) oxides. This analysis provides independent evidence for a significantly lower OH:O stoichiometric ratio for ferrihydrite than for goethite, further constraining the RMC models.

The *hybrid* structure model gave better agreement to the experimental total scattering data than nanoparticles based upon either the *Michel* or *Drits* models. Models that incorporated tetrahedrally coordinated iron sites consistently achieved better matches to the data than models containing face-sharing octahedra. Long-range vacancy disorder was essential for optimum fits to the scattering data, highlighting the utility of whole-nanoparticle models in place of unit-cell models with random distributions of iron vacancies. The RMC-derived structures do not satisfy all experimental constraints on composition and structure. Nevertheless this work illustrates that a suitably constrained RMC method applied to whole-nanoparticle models can be an effective approach for exploring disorder in nanocrystalline materials.

Keywords: Nanoparticle structure, reverse Monte Carlo, total X-ray scattering, pair distribution function

INTRODUCTION

Ferrihydrite is the name given to the iron oxyhydroxide nanomaterial that forms by hydrolysis in aqueous solutions of iron(III) (Cornell and Schwertmann 2003) in the absence of ions, such as phosphate, that interact strongly with ions and nucleating particles (Rose et al. 1996; Zhu et al. 2012). Although it is not the only environmental iron(III) (oxyhydr)oxide nanophase (van der Zee et al. 2003), it is of major geochemical importance because of its frequent occurrence in soils, sediments, and surface waters (Childs 1992; Waychunas et al. 2005); its large specific surface area and high affinity for aqueous ions including nutrients and contaminants (Fuller et al. 1993; Hochella et al. 2005; Cismasu et al. 2012); its role as a precursor in the formation of more stable

oxides and hydroxides (Jolivet et al. 2006); and its participation in the global iron redox cycle (Jickells et al. 2005; Stumm and Sulzberger 1992). Despite abundant empirical knowledge of the geochemistry of ferrihydrite, including formation conditions (Cornell and Schwertmann 2003; Guyodo et al. 2003), transformation pathways (Tronc et al. 1992; Pedersen et al. 2005), rates of microbial utilization (Bonneville et al. 2004), and surface adsorption phenomena (Dzombak and Morel 1990), underlying insight into the properties of this nanophase has been severely limited by uncertainty as to its atomic-scale structure. Thermodynamically unstable relative to alternative iron oxide and hydroxide phases (Majzlam et al. 2003), no macroscopic crystals of ferrihydrite have ever been synthesized and thus the derivation of structural models has predominantly been based upon powder X-ray diffraction (XRD) or high-resolution transmission electron microscopy

(TEM). Both particle size and crystallinity vary with synthesis conditions and consequently ferrihydrite samples are generally classified as either 2-line or 6-line on the basis of the number of resolvable peaks in standard XRD data.

For many years, the accepted description of the structure of ferrihydrite has been a multi-phase model developed by Drits and co-workers (Drits et al. 1993) developed from powder XRD data. Recently, Michel and co-workers proposed a single-phase model of ferrihydrite that was refined to real-space pair distribution function (PDF) data (Michel et al. 2007, 2010). There has been considerable debate as to the relative strengths of the *Drits* and *Michel* models (Manceau 2009, 2010, 2011; Rancourt and Meunier 2008) that illustrates important challenges of developing realistic atomistic models of nanoscale materials (Billinge and Levin 2007). In particular, the *Drits* and *Michel* models each achieve arbitrarily good agreement with, respectively, XRD and PDF data—but not with both. Seeking to understand this observation, we briefly review the two structural models and the use of X-ray scattering for analyzing the structure of nanoscale materials containing disorder.

TWO STRUCTURAL MODELS FOR FERRIHYDRITE

The *Drits* model

The basis of the *Drits* model is a hexagonal close-packed structure of anions (oxygen and hydroxide) that form planes between which octahedral sites are formed. Iron(III) cations reside at these octahedral sites with partial occupancy. Such an arrangement can incorporate stacking faults along the *c*-axis (the stacking direction). Drits et al. (1993) obtained good agreement in the position and relative intensities of the reflections observed in powder XRD by developing a statistical model describing the probabilities for alternative stacking configurations. Based on this approach, they identified two most prominent stacking configurations, designated the *defective* and *defect-free* phases (Figs. 1a to 1c), and proposed that these phases are the basis for all ferrihydrite materials. A very broad peak in the XRD data could not be reproduced by this crystalline two-phase model and was attributed to the presence of

a third phase, tiny crystallites of hematite. The three-phase *Drits* model has been supported by several independent investigations (Janney et al. 2001; Jansen et al. 2002), subject to slight variations of lattice parameters, site occupancies and the proportions of the different components.

The *Michel* model

The *Michel* model of ferrihydrite has the ideal stoichiometry $Fe_{10}O_{14}(OH)_2$ and is isostructural to synthetic tohdite and natural akdalaite. The unit cell is shown in Figure 1d. Michel et al. (2007) avoided the difficulties associated with size- and disorder-related XRD peak broadening by refining the structure to the real-space PDF. With minor variations in atomic positions and occupancies, Michel et al. obtained good agreement with PDF data from all samples studied, including both 2- and 6-line ferrihydrite and biological ferritin (Cowley et al. 2000; Liu et al. 2006); and the model is supported by neutron PDF analysis (Harrington et al. 2011) and ab initio simulation (Pinney et al. 2009). However, the *Michel* model fails to reproduce completely the accepted XRD pattern for 6LF (Rancourt and Meunier 2008).

Subsequently, Michel et al. (2010) analyzed the product of 2LF that was hydrothermally coarsened and annealed in the presence of surface-sorbing ions (e.g., citrate or phosphate), which prevented phase transformation. A low-disorder ferrimagnetic nanophase was formed prior to transformation to hematite. The resulting phase was termed ferromagnetic ferrihydrite, or *ferrifh*. This phase was considered to be identical to the postulated mineral nanoparticle termed *hydromaghemite* believed to be responsible for the magnetic susceptibility enhancement measured in certain soils (Barrón et al. 2003). Both the XRD and PDF data for the *ferrifh* phase are well described by the ideal *Michel* unit cell with close to ideal stoichiometry. Despite concerns about the formation pathway (Manceau 2011), the good agreement is strong evidence that the *Michel* model describes a genuine mineral phase. Michel et al. (2010) proposed all phases of ferrihydrite to be compositionally and structurally defective versions of *ferrifh*, with their revised description of the as-formed disordered phase having a significantly
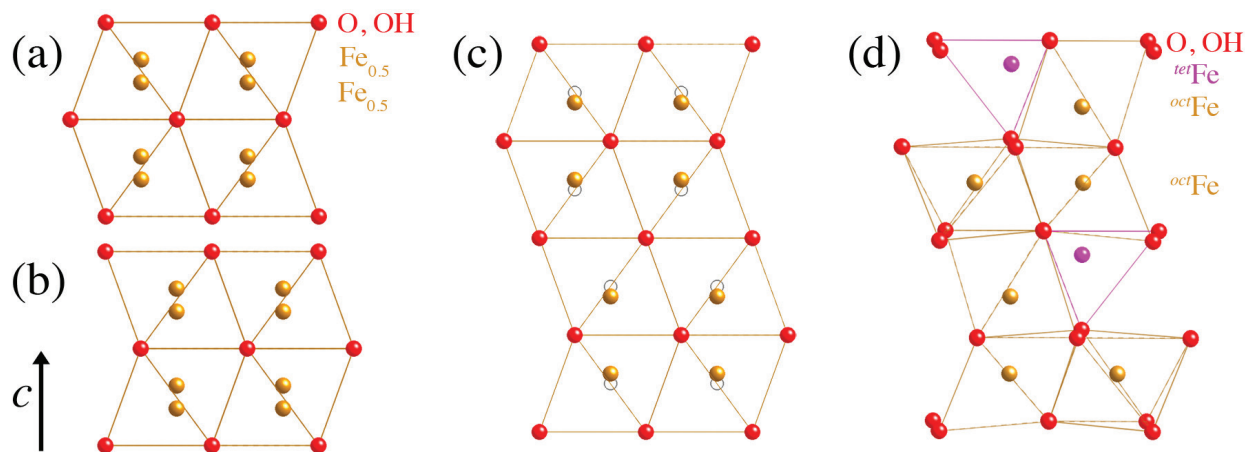
FIGURE 1. Comparison of *Drits* and *Michel* models for ferrihydrite. (**a** and **b**) The two orientations of the *Drits defective* phase. Multiple ½ occupancy Fe sites are shown. (**c**) The *Drits defect-free* phase, expanded two times in *a* to facilitate comparison with the *Michel* model. The iron sites are displaced in *c* away from the centers of the octahedra (black circles). (**d**) The *Michel* model. Protons are omitted. (Color online.)

lower iron occupancy that is consistent with the stoichiometry $Fe_{8.2}O_{8.5}(OH)_{7.4}$. However, the revised model does not achieve better agreement to the accepted XRD pattern for ferrihydrite.

The Michel model predicts a lower content of structural hydroxyl oxygen sites than expected for a material known to be highly hydrated (Manceau 2011). Knowledge of the OH:O ratio thus represents an important constraint on the structure of ferrihydrite (Xu et al. 2011; Hiemstra 2013). Experimental measurement of a low OH:Fe ratio (<0.18), compatible with the Michel model (0.2), was performed by in situ infrared (IR) spectroscopy during the thermal transformation of ferrihydrite to hematite (Xu et al. 2011). In this work, we show that O K-edge X-ray absorption spectroscopy provides an independent, although currently semi-quantitative, assessment of this question.

Relationship between the *Drits* and *Michel* models

Figures 1c and 1d compare the *Drits defect-free* phase with the *Michel* model. Both structures represent *ABACA*-type hexagonal packing of anions. The figure illustrates a key similarity: the distribution of octahedral Fe sites in the *Michel* model is one possible topological configuration that is permitted by the *defect-free Drits* model, which assumes essentially random occupancies. Two key features distinguish the models:

(1) The *Michel* model incorporates ~20% of iron atoms in tetrahedrally coordinated sites, ^{tet}Fe. Experimental demonstration of absence of this site would contradict the *Michel* model, but experimental detection and quantification of a fraction of $^{tet}Fe(III)$ sites in a predominantly $^{oct}Fe(III)$ mineral has long been challenging and controversial. Several recent complementary X-ray spectroscopic studies have presented evidence for ^{tet}Fe sites in ferrihydrite (Maillot et al. 2011; Peak and Regier 2012), with the strongest evidence being furnished by X-ray magnetic circular dichroism (XMCD) measurements (Guyodo et al. 2012). However, the interpretation of all such X-ray spectroscopic studies requires careful analysis and theoretical support and are not further evaluated here.

(2) The *defective* phase of the *Drits* model and the equivalent *double-chain* structure identified by Janney et al. (2001) contain a fraction of iron atoms in face-sharing octahedra (FSO). In bulk minerals containing FSO (e.g., hematite), a significant structural relaxation is observed that increases the cation-cation distance to values similar to those observed for edge-sharing octahedra (2.89–3.03 Å). Consequently, direct spectroscopic confirmation of a fraction of FSO configurations is even more challenging than identifying ^{tet}Fe sites.

Relationship between maghemite and the *Michel* model

Recently, Katz et al. (2012) found the cation-to-cation hopping rates of excess valence electrons in ~3 nm nanoparticles of 2-line ferrihydrite and maghemite to be indistinguishable, and significantly different from the hopping rate in hematite. This finding suggests that ferrihydrite and maghemite possess similar crystal chemistry, and thus we compared the maghemite structure with literature models for ferrihydrite. The *Michel* structure is closely related to maghemite, γ-Fe_2O_3 (Greaves 1983) as can be seen by comparing stacking of ^{oct}Fe layers in the ferrihydrite (001) and maghemite (111) directions (Figs. 2a and 2b). The octahedral framework of either phase may be constructed by stacking an

identical two-dimensional unit consisting of two planes of iron atoms, which we denote the *bridging* and *continuous* layers, which are joined together by edge-sharing links (Fig. 2c). The maghemite framework may be expanded along its (111) direction by forming new face-sharing links between iron octahedra in the bridging and continuous layers. The *Michel* model may be expanded along its (001) direction by forming corner-sharing links (Fig. 2d). Tetrahedrally coordinated iron atoms occur at equivalent locations in the two structures, with one triangular side forming three corner-sharing links at the locations of the voids in the continuous layer. However, because the bridging octahedra occupy all such locations on one side of each continuous layer in the *Michel* model, this structure has half as many ^{tet}Fe sites and they are all oriented in a single direction. The introduction of a *maghemite* stacking arrangement into a structure based on the *Michel* model can create a twin plane with mirror symmetry with the orientation of the tetrahedral sites inverted. As reported below, we investigated the effect of simple *maghemite-Michel* stacking faults on the calculated XRD patterns.

TOTAL SCATTERING ANALYSIS OF DISORDERED AND NANOSCALE MATERIALS

Relationship between diffraction and pair distribution function data

In principle, diffraction and PDF data, which may be obtained by either X-ray or neutron scattering experiments, are simply alternative forms of the same measurement, related by a Fourier transform (Guinier 1967). However, Bragg peaks in diffraction data are highly sensitive to periodic long-range structure and Bragg analysis of diffraction data can overlook short-range structural distortions that contribute diffuse scattering intensity between and at the base of Bragg peaks. The transformation of the total wide-angle X-ray scattering pattern to generate the real-space PDF captures information about short-range structure, including disorder. Crystalline periodicity can be inferred from PDF data provided long-range atom-atom pair correlations (on the length scale of several unit cells) are obtained. However, the PDF method requires high-angular resolution to detect distant atom-atom pair correlations (Toby and Egami 1992), while two-dimensional detectors that are now most commonly used for PDF analysis do not provide the highest angular resolution (Chupas et al. 2007). Thus, simultaneous consideration of both the reciprocal and real-space forms of total scattering data are required for assessing structural models at the widest range of length scales (Dove et al. 2002).

Total scattering studies of disordered materials

The total scattering method has been widely used for the structural characterization of amorphous materials, including liquids (Head-Gordon and Hura 2002), glasses (Wright 1988), amorphous mineral phases (Keen 1998; Goodwin et al. 2010), and molecular structures including pharmaceutical compounds (Bates et al. 2006) and metal-inorganic framework materials (Bennett et al. 2010). Use of the reverse Monte Carlo method (Keen and McGreevy 1990) is straightforward for such materials, enabling the generation of atomistic structural models that can give insight into static structure such as ring topologies or conduction pathways within glasses (Norberg et al. 2009).
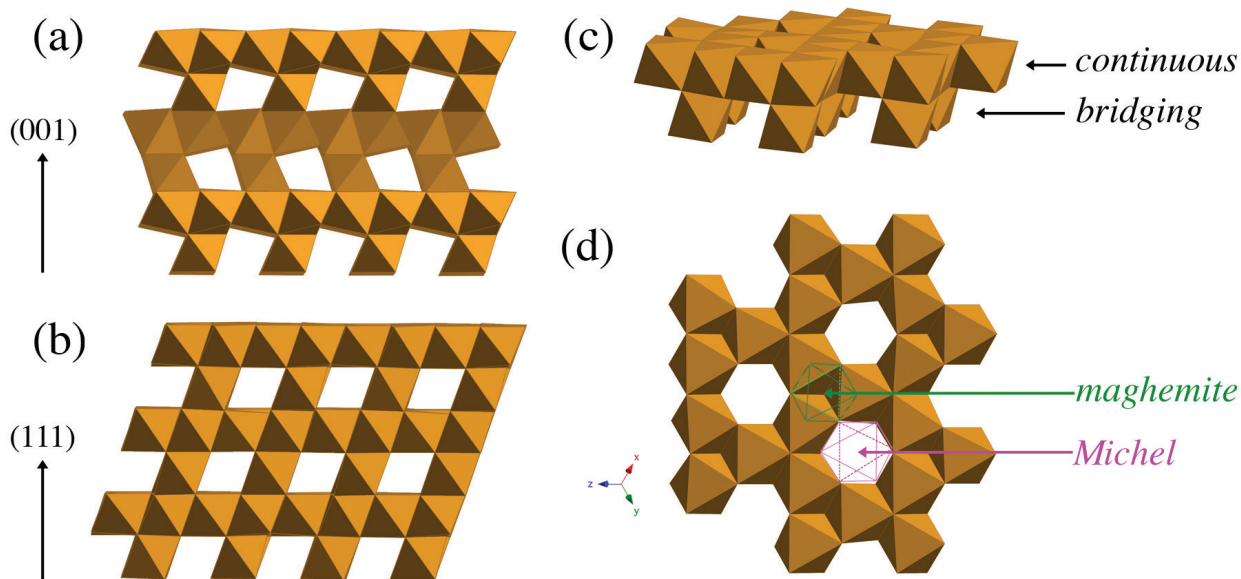
FIGURE 2. Comparison of the stacking geometry of the octahedral iron sites in (**a**) the *Michel* model and (**b**) maghemite. Tetrahedral iron sites are not shown for clarity. (**a** and **b**) The structure seen perpendicular to the stacking axes (arrows). The octahedral iron framework of each phase can be constructed by the same two-layer fragment, shown in (**c**), with bridging octahedra attaching to the continuous layer at the locations of the in-plane rotations shown in (**d**). (Color online.)

The use of total scattering methods to analyze the structures of crystalline materials containing disorder is relatively recent. Single unit-cell and RMC-based refinements have provided sensitive determination of short-range features difficult to determine from Bragg analysis of XRD data (Paglia et al. 2006; Billinge et al. 1996; Shoemaker et al. 2009). Extension of the RMC approach has been of particular utility in revealing dynamic aspects of crystal structure (Proffen and Neder 1997; Tucker et al. 2001), such as the temperature dependent motions of structural groups in negative thermal expansion material (Tucker et al. 2005). Numerous models of crystalline disorder, including defects, short-range distortions, and stacking faults can be optimized with appropriate methods (Proffen and Neder 1997).

Total scattering studies of nanomaterials

Total scattering studies of nanomaterials have typically refined a set of unit-cell parameters for a specific phase, often finding the presence of strain within nanocrystals (Gilbert et al. 2004; Masedeh et al. 2007). Nanomaterial morphology exerts a detectable effect on total scattering data (Gilbert 2008; Harrington et al. 2012), and nanomaterials with complex and highly anisotropic morphologies have been studied in this way (Petkov et al. 2004). There are very few reports of the use of whole-nanoparticle models for structural optimization. Page et al. (2011) constructed a fully atomistic model of a ligand-capped gold nanoparticle and demonstrated the refinement of five global structural parameters. The whole-nanoparticle RMC approach has been used to explore disordered atomic positions in 3 nm diameter amorphous titania nanoparticles (Zhang et al. 2008) and crystalline but disordered ruthenium nanoparticles (Bedford et al. 2007).

A whole-nanoparticle reverse Monte Carlo approach

Here we describe a novel structural analysis of total X-ray scattering data acquired from 6-line ferrihydrite prepared by a highly standardized synthesis method (Guyodo et al. 2003; Erbs et al. 2008). In contrast to prior work, we generate whole-nanoparticle atomistic models of ferrihydrite (including defects and disorder) and quantitatively evaluate the ability of candidate structures to reproduce *both* the reciprocal and real-space forms of the X-ray scattering data. We implemented a reverse Monte Carlo approach to explore alternative configurations of iron occupancies on a virtual lattice that was based on the *Drits defect-free* phase but additionally incorporated ^{tet}Fe sites (Fig. 3) (Gilbert 2009; Maillot et al. 2011). This approach cannot fully test the concept of Drits et al. (1993) that ferrihydrite is a multi-phase intermix, and the approach is counter to the idea that ferrihydrite inherently contains individual particles of distinct phases (Drits et al. 1993; Marchand and Rancourt 2009). Nevertheless, full-nanoparticle models can incorporate explicit types of structural variation that are not easily described by single unit-cell models. In particular, the approach allows explicit distributions of occupied and unoccupied iron sites at a nanometer scale, enabling new topologies to be explored in ways that cannot be captured by assigning a fractional occupation probability to sites within a single cell.

METHODS

Ferrihydrite synthesis

Six-line ferrihydrite samples were prepared using the method of Penn et al. (2006), shown to produce nanoparticles with no impurity phases, and with mean particle diameters that can be varied between 3.4–5.9 nm with a relative standard deviation of 12% or better. Ferrihydrite suspensions were prepared by the controlled addition of a 0.48 M NaHCO$_3$ (Mallinckrodt) solution to an equal volume of 0.40 M

Fe(NO$_3$)$_3$·9H$_2$O (Fisher) with vigorous stirring at 4, 23, 45, 66, or 80 °C. The base solution was added over 12 ± 1 min using a Fisher peristaltic pump. Suspensions prepared at 45, 66, or 80 °C were immediately submerged in an ice bath to cool to room temperature. Each suspension was then microwave-annealed (950 Watt oven) for 30 s intervals until boiling and then rapidly cooled by submerging the reaction bottle in an ice-water bath. Dialysis (Spectra-Por no.7 dialysis bags, MWCO = 2000 g/mol) against Milli-Q water was performed at 10 °C for three days, changing the water a minimum of nine times. One-quarter of each suspension was kept at 10 °C for reaction without drying, and such samples are hereafter referred to as freshly prepared suspensions. The other portion was allowed to air-dry for five days, ground into a powder using an agate mortar and pestle, and stored in glass vials. The size and morphology of the particles were analyzed from calibrated TEM images collected using an FEI Tecnai T12 TEM, operated at 120 kV, and a Gatan CCD camera (Erbs et al. 2008). Using Gatan Digital Micrograph 3.8.2, the lengths of more than 500 particles were measured.

X-ray diffraction (XRD) analysis

We performed powder XRD at the Advanced Light Source (ALS), Lawrence Berkeley National Laboratory, beamline 11.3.1 using 17.0 keV X-rays (0.7293 Å). Dried powders were mounted on Kapton and XRD was performed in transmission using a two-dimensional (2D) detector (Bruker). The scattering geometry was calibrated using a LaB$_6$ standard and the 2D data were integrated onto a 2θ axis the program Fit2D (Hammersley 1997).

Pair distribution function (PDF) analysis

We acquired wide-angle X-ray scattering data at 90 keV from powdered samples placed inside a hollow Kapton tube at beamline 11-ID-C of the Advanced Photon Source at Argonne National Laboratory using a Mar 2D image plate detector. We acquired between 10 and 15 two- or five-minute exposures from an empty tube and each sample, respectively. Fit2D was used to calibrate the detector geometry using data acquired from a Si standard to bin each 2D pattern onto a 1D q axis.

The structure factor for each iron oxide was obtained using the program RAD to subtract the Kapton background and the coherent and Compton atomic scattering contributions (Petkov 1989). The PDF was generated by applying a sine transformation to the q-weighted data up to $q_{max} = 27$ Å^{-1}. We used the PDFGui code (Farrow et al. 2007) to fit the data from a bulk hematite reference sample to the real-space data between 1–32 Å. This fit provided parameters describing the finite data effect and the quadratic correction for correlated atomic motion that were used for the RMC analysis of the nanoparticle samples.

Oxygen K-edge absorption spectroscopy

Portions of air-dried and finely ground bulk hematite, goethite, and maghemite and 6-line ferrihydrite nanoparticles were pressed into indium for soft X-ray spectroscopy analysis under vacuum. Oxygen K-edge X-ray absorption studies were performed at beamline 7.0 at the ALS with the incident X-ray energy resolution better
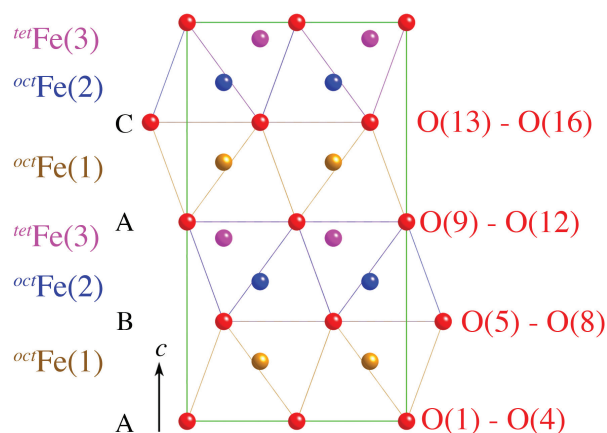
than 0.2 eV. The absorption spectra were acquired in both fluorescence and total electron yield simultaneously and were calibrated by applying a linear transformation to the energy axis to align the spectrum obtained from a TiO$_2$ (anatase) standard to a published reference (Lusvardi et al. 1998). Following this correction, the inflection point of the onset of the bulk hematite absorption spectrum was measured to be 529.7 eV, in good agreement with recent studies (Gilbert et al. 2009; Prince et al. 2005). The absorption spectra were normalized for the energy dependence of incident beam intensity by the division of a gold grid electron yield signal acquired simultaneously with the sample, and then scaled to unity step jump at 552.5 eV.

Reverse Monte Carlo

We created a reverse Monte Carlo (RMC) code using the IgorPro software to create single nanoparticle models (a set of iron and oxygen atom coordinates) incorporating both occupied and unoccupied lattice sites; simulate the X-ray scattering functions (Keen 2001), the structure factor, S(Q) (equivalent to the XRD pattern), and the pair distribution function, G(r) (also called the PDF); and generate modified configurations (subject to optional constraints) by relocating atoms between sites and by applying random displacements. The standard RMC method is used to assess new configurations, accepting all changes that improve agreement to data as well as a fraction of those that do not according to the Metropolis algorithm. The X-ray scattering calculations are standard, using approaches that are described fully in the literature. Briefly, the X-ray scattering is calculated using the Debye equation (Guinier 1967; Rancourt and Meunier 2008), incorporating the relevant atomic form factors. The PDF is calculated as a sum of Gaussian-broadened atom-atom correlations, incorporating experimentally determined parameters that account for the finite Q-range and detector angular resolution (Proffen and Billinge 1999). The smooth PDF background is derived from an analytical expression for a sphere that was optimized once from the PDF data (Gilbert 2008). The full array of $N(N-1)$ atom-atom correlations is calculated once, at the start of a run. Following every RMC move, only the changed partial correlations and scattering functions associated with displaced atoms are calculated.

RMC approach

All RMC models were 3.6 nm diameter spherical particles (approximately 800 iron atoms) with all iron sites fully coordinated by oxygen atoms. Prior to the RMC run, the ratio of occupied-to-unoccupied iron sites was varied until the target density for the structure was achieved. RMC runs were typically run for 10 to 50000 iterations (~50 iterations per hour on a MacPro 3.1 with two 3-GHz QuadCore processors); up to four ran in parallel. A single RMC move involved the relocation or displacement of a number of atoms (typically 20), modification of the S(Q) and G(r) functions, and calculation of the change in the goodness of fit, χ^2, defined as:

$$\chi^2 = \{\Sigma_i[S(Q_i)_{exp} - S(Q_i)_{calc}]^2 + \Sigma_i[G(r_i)_{exp} - G(r_i)_{calc}]^2\}/\sigma^2.$$

RCM moves that increased χ^2 were accepted with a probability $P = \exp(-\Delta\chi^2/2)$. The weighting factor, σ, was varied to adjust the proportion of unfavorable moves that were accepted; about one third of all accepted moves were unfavorable. If the composite move was rejected, all atoms were returned to their starting positions.

Relocation (swap) moves. One occupied iron site was selected at random, then a second, unoccupied site found. Provided that occupying the latter site would not violate any atom-atom distance constraints, the selected iron atom was moved.

Displacement moves. One type of oxygen or iron site was chosen at random and a vector of random orientation and with a magnitude selected randomly from a Gaussian distribution with a mean of 0.05 Å and a FHWM 0.02 Å. Several occupied sites of that type were found randomly in the structure and displaced with the same vector (subject to nearest neighbor constraints). Optionally, if $\Delta\chi^2 < 0$, a new set of atoms of the same type was found and displaced, until all occupied sites of that type had been moved, or until $\Delta\chi^2 \geq 0$. This loop through all occupied sites of a given type crudely allowed changes in the underlying unit cell to be propagated throughout the structure.

RMC structures

Simplified *Drits* phase nanoparticle. We created nanoparticles based on a simplified version of the Drits model. We sought to test whether the presence of face-sharing octahedra (FSO) sites (without tetrahedral sites) was a key structural component. The nanoparticle was constructed from fixed proportions of *defective* and *defect-free* structure in a single model with stacking faults. Reported proportions of these phases range from 2:1 (Drits et al. 1993; this study) to 1:1 (Jansen et al. 2002). According to Drits et al. (1993), the two phases tend to segregate, and thus we created

FIGURE 3. Side view of the overfilled unit cell of the *hybrid* model containing three distinct iron sites and 16 distinct oxygen sites. Atomic coordinates are given in Supplemental Table 1[1]. (Color online.)

nanoparticles of the form $(ABACA)_n$ plus a mixture of ABA and ACA sequences. A challenge for this model is to account for the structural relaxation of pairs of iron sites in FSO [see Fig. 1 in Manceau (2011)]. Without incorporating force fields, the RMC approach does not naturally consider correlated displacements of this type. To account for this, we created three possible lattice sites within each iron octahedral site. Occupation of the central position would be expected for non-face-sharing site; occupation of the lower (upper) position would be expected if the neighboring ^{oct}Fe site above (below) this one was full.

Michel phase nanoparticle. We created two nanoparticles using the *ferrifh* structure and introduced 10% or 30% iron vacancies among the Fe(2) and Fe(3) sites. We tested whether occupational disorder and atomic displacements within a nanoparticle model could improve agreement with the X-ray scattering data relative to a single unit-cell model.

Hybrid phase nanoparticle. We created a lattice of iron and oxygen sites that is identical to the *defect-free* Drits model with the addition of ^{tet}Fe sites in all locations suggested by the *Michel* model (Fig. 3 and Supplemental Table 1[1]). Thus, while the Michel model described two ^{tet}Fe sites per unit cell, the hybrid model permits eight. This approach was also proposed by Maillot et al. (2011).

RMC constraints

Atom relocations and displacements were rejected if they violated limits on acceptable distances between atoms (Keen 1998). The minimum permitted distance for any pair of atoms was 1.6 Å. Face-sharing configurations of pairs of octahedra or between tetrahedral and octahedral sites were excluded by setting both $d_{min}(^{oct}Fe—^{oct}Fe)$ > 2.3 Å and $d_{min}(^{oct}Fe—^{tet}Fe)$ > 2.3 Å. Clustering of tetrahedral sites was prevented by setting $d_{min}(^{tet}Fe—^{tet}Fe)$ > 4.0 Å. For these constraints, unoccupied sites were not considered. In addition, no displacement was accepted if it changed the coordination number of the displaced atom; both occupied and unoccupied sites were considered.

RMC nanoparticle structure analysis

Following a run, non-bonded oxygen atoms were removed and the scattering functions recalculated. Removal of non-bonded atoms had negligible effect on the goodness-of-fit. The resulting structure was analyzed as follows. To avoid difficulties in calculating the volume of the nanoparticles following RMC, we calculated a density function, $\rho(r)$, where r is the radius of a sphere about the most central atom. The nanoparticle density was estimated at the limit $r \rightarrow r_{max}$. An analogous function for the stoichiometric Fe:O ratio was calculated to reveal surface effects on this parameter.

Surveys of solved crystal structures have revealed strong chemical constraints on the coordination environment of atoms in crystals (Brown and Altermatt 1985). These constraints can be expressed as expectations for bond lengths (for specific metal-ligand geometries and metal oxidation states) and by the bond valence approach (Brese and O'Keeffe 1991). The bond valence, s_{ij}, contributed to an atom i by its ligand j, is defined as $s_{ij} = \exp[(r - r_o)/0.37]$ in valence units (v.u.), where the empirical parameter $r_o = 1.76$ for iron(III)-oxygen bonds. For stable bulk crystal structures, the valence of an atom should be equal to the sum of bond valence contributions from its ligands.

RESULTS AND DISCUSSION

X-ray diffraction

Figure 4 reports XRD data for all 6LF samples and Rietveld refinement of the data from 6 nm 6LF using the 3-phase *Drits* and the *Michel* models. Both models fitted similar values of the *c* parameter. The *Drits* model provided the better fit to the XRD data, although a poorer fit is achieved than reported by Drits et al. (1993) likely because we fitted a discrete mixture of phases, rather than a statistical model of coherent stacking arrangements. All XRD patterns based on the *Michel* model exhibited discrepancies as described by Rancourt and Meunier (2008) that could not be resolved by varying any combination of occupancies, thermal factors or atomic displacement, or by incorporating peak broaden-

ing based on anisotropic particle morphology. Neither model was able to accurately reproduce the distinct splitting evident in both the main peaks. The fitted unit-cell dimensions, a = 5.92 Å and c = 9.3 Å, were used for generating RMC structures.

The relationship between the *Michel* and *maghemite* phases indicates that stacking faults might form easily, allowing mixed phase structures as is frequently seen for materials possessing *hexagonal-cubic* polytypism. Indeed, a *Michel/maghemite/Michel* twinning plane can be generated that leads to an inversion of the direction of the tetrahedral sites in the *Michel* phase. We investigated the effect of *Michel/maghemite* stacking faults and tested the consequences for the PDF and S(Q) data. The incorporation of *maghemite* domains in the *Michel* model never improved agreement with XRD (Fig. 4d). Thus, although we do not rule out the presence of maghemite domains in natural ferrihydrite, we did not further consider that possibility in this work.

Oxygen X-ray absorption spectroscopy

Recently, oxygen K-edge X-ray absorption spectra of ferrihydrite powders suggested that this approach is sensitive to the relative abundances of protonated and non-protonated oxygen sites in a metal oxide (Erbs et al. 2008), which we explored further. Figure 5 reports oxygen K-edge X-ray absorption spectra acquired from powders of reference iron (hydr)oxides and 6 nm 6LF. Each spectrum exhibits pre-edge peaks in the 528–534 eV region that represent transitions from O 1s to Fe 3d states. For the oxides hematite and maghemite, the Fe 3d states are split by the octahedral crystal field, forming two distinct e_g and t_{2g} states. The pre-edge structure for these phases was well fitted by a doublet composed of two Gaussians (Table 1). For goethite, there are two O 1s states, corresponding to the protonated (OH) and non-protonated (O) sites in the lattice. The protonation of structural oxygen atoms leads to a chemical shift in the O 1s binding energy and a total of four 1$s \rightarrow 3d$ transition energies. The pre-edge structure for goethite was well fitted by two doublets with the ratio of integrated areas 0.55:0.45, close to the expected 50:50. The spectrum for 6LF is intermediate, with the fit results indicating approximately 10% of O atoms are protonated, although the accuracy of this estimate is unknown. Studies of the size-dependence of O K-edge XANES from 6LF showed that a higher surface area correlated with a higher signal from OH groups (Erbs et al. 2008), but this does not alter the main conclusion of a significantly lower structural hydroxyl content in ferrihydrite than in goethite.

Reverse Monte Carlo study

We performed 48 independent RMC runs starting from one of the three structural models described above. RMC nanoparticles of diameter 3.6 nm were refined to data from the 5.9 nm diameter 6LF sample, which exhibited the best-resolved peaks in the X-ray scattering patterns. Figure 6 displays the trends in the RMC χ^2 goodness of fit parameter for selected runs for each structure. Figure 7 compares initial and final scattering curves for the *Michel* and *hybrid* structures. Figure 8 presents several views of a *hybrid* model nanoparticle after RMC refinement (pink curve in Fig. 7).

The *Michel* model gave the best initial match to data. However, exploring iron occupation disorder in the Michel model did not significantly improve agreement with S(Q) (arrows 1 and 2, Fig. 7). In 20 000 iterations, only ~20 RMC relocation moves improved

---
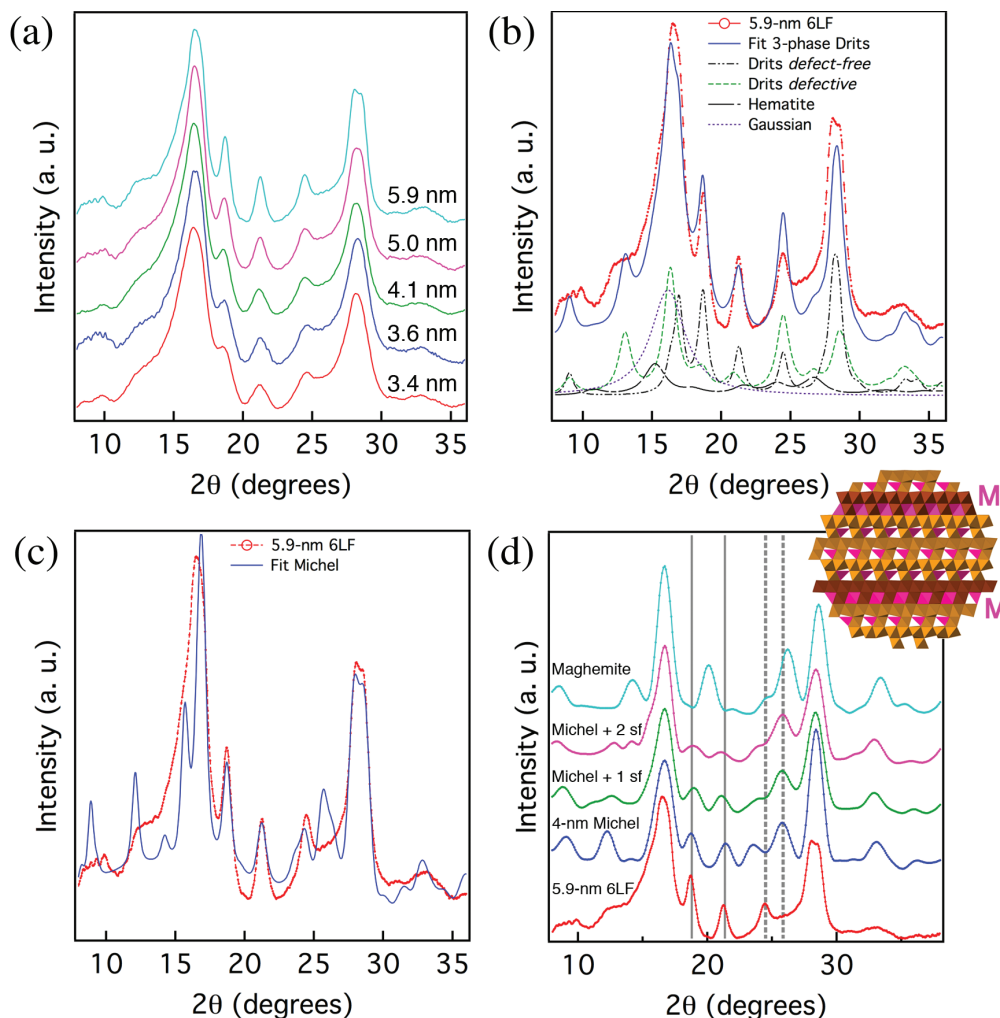
FIGURE 4. Synchrotron powder X-ray diffraction (XRD) study of 6-line ferrihydrite (6LF) samples. (**a**) Background subtracted XRD data from all 6LF samples. (**b**) Best-fit refinement of 3-phase *Drits* model to the XRD data for 6 nm 6LF. (**c**) Best-fit refinement of *Michel* model to 6 nm 6LF data. (**d**) Investigation of the effect of incorporation of *maghemite/Michel* stacking faults (sf) into *Michel* model of a 3.6 nm nanoparticle. Inset: Cross-section view of a *Michel* model nanoparticle with two *maghemite* (M) layers. (Color online.)

χ^2. After these moves were found, χ^2 grew due to the accumulation of unfavorable moves. Our single-nanoparticle implementation of the *Drits* model gave a poor initial match to data. Both relocation and displacement moves produced steady improvement, but for all RMC runs with our *Drits* nanoparticles, χ^2 throughout an RMC was always significantly greater than either the *Michel* or *hybrid* models.

In all RMC runs, the *hybrid* model underwent rapid initial improvement due mainly to successful relocation moves, followed by steady improvement associated with displacement moves. For the run reported below, out of 10 000 RMC steps, 244 favorable and 180 unfavorable relocation moves were accepted, and 36 030 and 31 694 favorable and unfavorable displacement moves. The rate of convergence (as well as some structural details) depended on the number and type of constraints on interatomic distances. In almost all cases, the *hybrid* model structure converged to a slightly lower χ^2 than the best agreement attained for the *Michel* model.

The *hybrid* model—Comparison with X-ray scattering data

The *hybrid* model achieved better agreement than the *Michel* model with the S(*Q*) data in the 3–5 Å^{-1} range. Moreover, the *hybrid* model developed asymmetric broadening in the main diffraction peak around 2.5 Å^{-1}, although this model did not always reproduce the correct peak intensity (arrow 3, Fig. 7). Drits et al. (1993) invoked the presence of tiny hematite nanocrystals to account for such broad diffraction peaks. However, neither Janney et al. (2001) (electron nanodiffraction) nor Jansen et al. (2002) (neutron scattering) found evidence of the hematite phase in 6-line ferrihydrite. RMC exploration of Fe occupancies and positional disorder in the *Michel* model did not lead to asymmetric peak broadening in this region (arrow 4, Fig. 7).

The calculated PDF curves for the *hybrid* model always underestimated the intensity of the peak at 5.4 Å (arrow 5, Fig. 7). In the starting structure, this peak is dominated by Fe(1)-Fe(1) and Fe(1)-Fe(2) distances, possibly indicating that the predicted Fe(2)
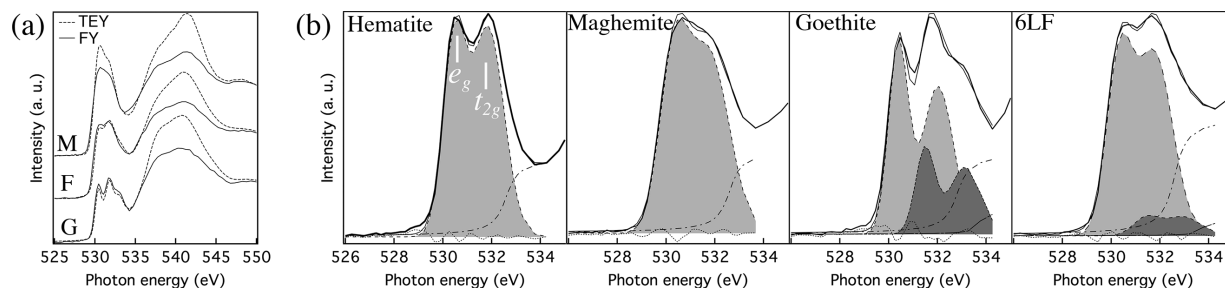
FIGURE 5. Oxygen *K*-edge absorption spectra from iron oxide and hydroxide references and 6 nm 6-line ferrihydrite (6LF). (**a**) Comparison of spectra acquired in total electron yield (TEY) and fluorescence yield (TY) from nanocrystalline maghemite (M), 6LF (F) and goethite (G). (**b**) Results of fits to the pre-edge region of the oxygen *K*-edge spectra. Light and dark shaded doublets represent contributions from transitions involving O and OH atoms, respectively.

TABLE 1. Results of fitting one or two Gaussian doublets to the O *K*-edge absorption spectra pre-edge peaks between 528–534 eV for the indicated phases

	Hematite	Maghemite	Goethite	6LF
O 1s → Fe 3d				
E (t_{2g}) (eV)	530.47 (0.02)	530.32 (0.02)	530.40 (0.03)	530.34 (0.03)
ΔE (t_{2g}–e_g) (eV)	1.39 (0.02)	1.44 (0.03)	1.63 (0.04)	1.44 (0.03)
I(e_g)/I(t_{2g})[a]	1.5	1.5	1.25	1.5
FWHM (t_{2g}) (eV)	0.47	0.59	0.41	0.53
FWHM(e_g)/FHWM(t_{2g})[a]	1.4	1.4	1.6	1.4
Area (OH 1s)/Area (O 1s)	–	–	0.45 (0.06)	0.10 (0.06)

Notes: Shown are the parameters for the O 1s → Fe 3d component. For samples containing protonated oxygen atoms, one additional doublet was fitted for the OH 1s → Fe 3d component. The OH doublet was constrained to have the same peak width, splitting, and ratio of peak intensities as the O doublet. Numbers in parentheses are the errors in the fit values obtained from non-linear least-squares fitting.
[a] The ratios of e_g to t_{2g} peak intensities and peak widths were fixed at the values shown.

occupancy was too low. However, we found that the strength of this peak is also affected by the precise distances between Fe(1) and oxygen atoms O(1–4) and O(9–12), as discussed further below.

Several other discrepancies are likely due to limitations in the modeling approach. The first three PDF peaks are overly broadened due to the accumulation of random disorder. Fine structure in S(Q) is missing for Q > 12 Å⁻¹, likely due to excess disorder introduced from the random RMC displacements and because the model nanoparticle (3.6 nm) is smaller than the mean sample particle size (5.9 nm).

The *hybrid* model—Composition

Evaluation of the RMC-derived structures must include comparison with unit-cell models and to experimental data. However, as described by Hiemstra and Van Riemsdijk (2009) and Hiemstra (2013), there are challenges associated with both because the whole-nanoparticle models contain excess surface oxygen atoms relative to a unit-cell model. Figure 9 shows our method to distinguish total and interior stoichiometry. Because the RMC-derived structures are not intended to represent actual 6LF nanoparticles, we principally analyze the core region, and do not consider surface modifications such as a site-depletion model (Hiemstra 2013).

The density of the nanoparticle core is 4.36 g/cm⁻¹, higher than several values reported for highly disordered ferrihydrite but less than the ideal value for annealed ferrihydrite (4.9 g/cm⁻¹). Because the number of Fe site vacancies in the starting structure
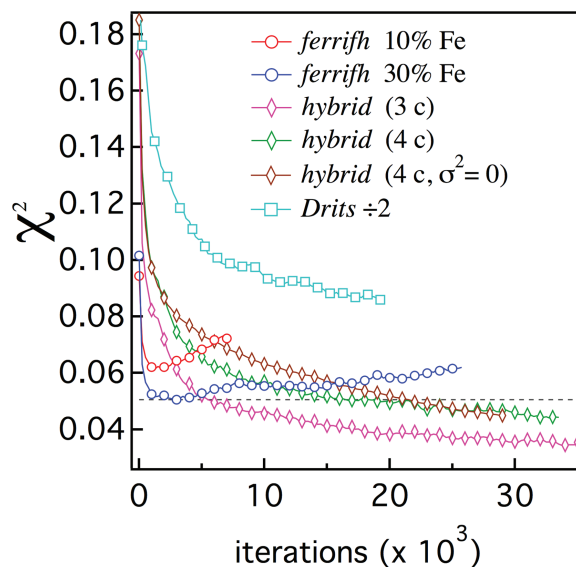
FIGURE 6. Evolution of the χ^2 goodness of fit parameter during selected RMC runs for 3.6 nm diameter nanoparticles constructed from the indicated phases. Each iteration reported in this plot represents one attempt to relocate 20 Fe atoms, and one or multiple cycles of displacing 20 Fe or O atoms of a certain site number with the same randomly generated displacement vector. "3 c" indicates that three constraints on atom-atom distances were applied. $\sigma^2 = 0$ indicates the RMC run did not permit any unfavorable moves. The χ^2 values for the *Drits* nanoparticle were divided by 2 for clarity of display. (Color online.)

was chosen to achieve a density closer to the experimental values, both initial and final structures contain evident internal porosity. The dimensions of voids in the Fe(1) *continuous layer* (cf. Fig. 2) reached up to 9 Å in two RMC nanoparticles. However, there was little obvious difference in the size and distribution of internal pore structure among RMC nanoparticles refined to the data and nanoparticles for which 2000 RMC moves were applied randomly without comparison to data. The suggestion that ferrihydrite nanoparticles are internally porous is in accord with several observations. Ferrihydrite is known to readily incorporate large impurity ions when it precipitates rapidly from aqueous solution (Fuller et al. 1993). Such species cannot occupy lattice sites and could be accommodated by internal pores. Moreover,
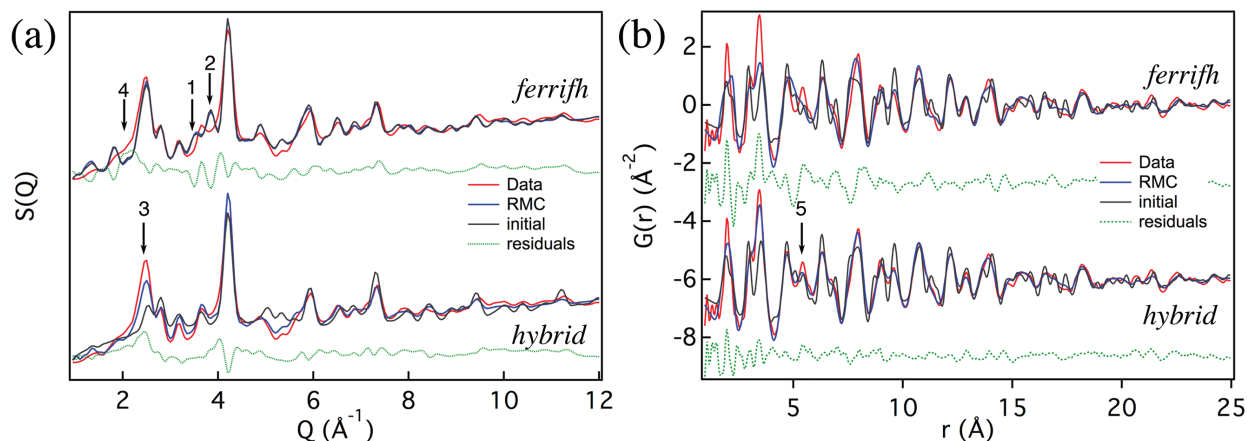
FIGURE 7. Red curves are the (**a**) structure factor and (**b**) pair distribution function data for 5.9 nm diameter 6-line ferrihydrite nanoparticles. Gray curves are calculated from initial model nanoparticle structures based on the *ferrifh* and *hybrid* models used for RMC refinement. Blue curves are calculated from nanoparticle structures that gave the minimum χ^2 obtained during a RMC run. Green curves give the residuals. Discrepancies highlighted by numbered arrows are discussed in the text. (Color online.)

thermochemistry studies have shown ferrihydrite to have the lowest surface enthalpy among the iron (oxyhydr)oxides (Navrotsky et al. 2008), indicating that a high-internal surface area could be energetically possible.

Considering the number of protons required for charge neutrality, the stoichiometry is $Fe(1)_{416}Fe(2)_{214}Fe(3)_{129}O_{1700}H_{1123}$, with an overall Fe:O ratio of 0.45. However, this formula treats the RMC structure as a real, hydrated nanoparticle that must contain an unknown proportion of unprotonated oxygen atoms, OH groups, and water molecules. As shown in Figure 9, we estimated the Fe:O ratio of the structure interior to be 0.55, corresponding to a charge-neutral formula of $Fe_{0.55}O_{0.82}(OH)_{0.18}$. This Fe:O ratio is larger than value 0.51 reported by Michel et al. (2010) for the revised *fhyd* structure. The OH:Fe ratio is 0.35, larger than the value 0.18 reported by Xu et al. (2011). The OH:O ratio is 0.18, larger than or our own estimate based on oxygen X-ray absorption data. Thus, although the RMC structure better reproduces the scattering data, it does not satisfy experimental constraints on composition. For the present models, the requirement of low OH content is more easily satisfied by fewer Fe vacancies, while obtaining a better match to the low expected mass density suggests more Fe vacancies (leading to interior porosity). The RMC refinements were not able to simultaneously satisfy these two constraints.

The *hybrid* model—Structure

The RMC runs predicted a range of tetrahedral site occupancies in the range 15–30%, with a strong dependence on Fe-Fe distance constraints. Initial runs predicted a high occupancy of ${}^{tet}Fe$ sites (up to 32%). Setting $d_{min}({}^{tet}Fe—{}^{tet}Fe) > 4.0$ Å prevented clustering of these sites and lowered the occupancy to less than 20%. This constraint increased the χ^2 value, which nevertheless remained lower for this model than any other.

The RMC structures exhibited a broad distribution of bond lengths for all sites. Almost all iron-oxygen bond length distributions were symmetric with mean values close to those expected from surveys of crystal structures. For the structure of Figure 8, the mean ${}^{oct}Fe(1)$–O bond length is 2.028 Å, compared to the expected 2.015 Å. The mean ${}^{tet}Fe(3)$–O bond length is 1.806 Å, compared
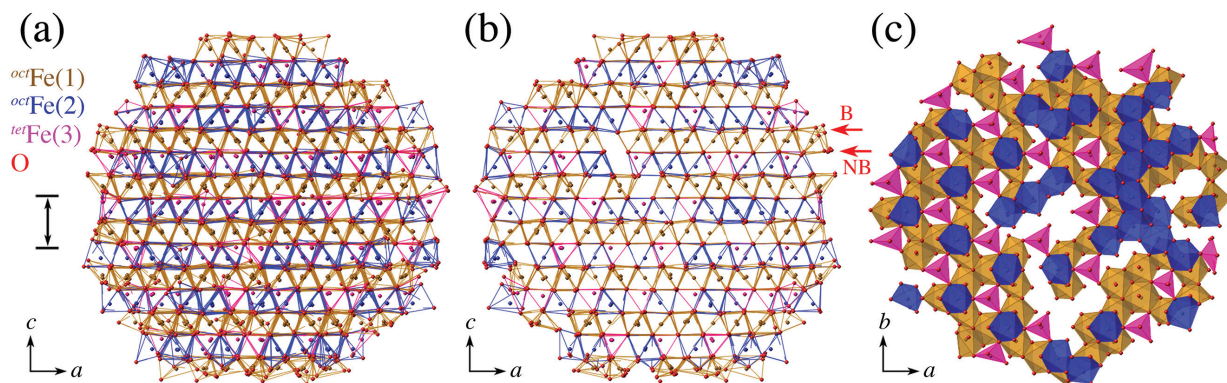
FIGURE 8. Views of the 3.6 nm *hybrid* model nanoparticle after RMC refinement. (**a**) Complete nanoparticle. (**b**) Cross section in *a-c* plane. Arrows labeled "B" and "NB" indicate planes of buckled and non-buckled oxygen sites, respectively. (**c**) Cross section in *a-b* plane to reveal disordered arrangements of iron octahedra and tetrahedra, as well as interior pores. (Color online.)
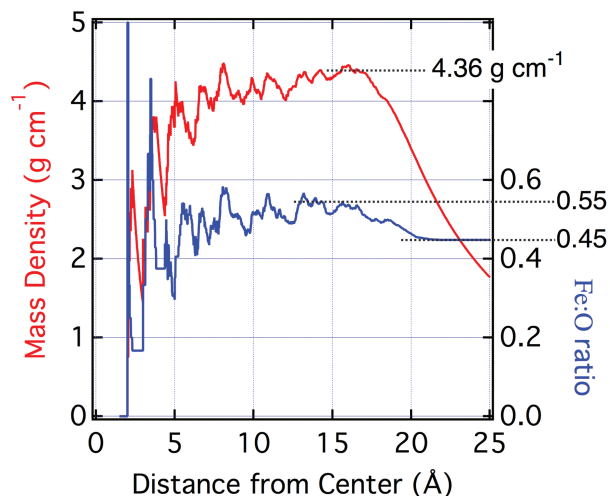
FIGURE 9. Illustration of the method for estimating the mass density and Fe:O elemental ratio for RMC derived ferrihydrite nanoparticles. (Color online.)

to the expected 1.865 Å. However, the $^{oct}Fe(2)$–O bond length distribution was bimodal with one distribution centered at 2.000 Å, Additionally, the Fe(2) bonds to oxygen atoms in two planes, O(1–4) and O(9–12) formed a second distribution centered at 2.224 Å. This bond length is anomalously long, and is the second major discrepancy involving these two planes of atoms. These planes of oxygen atoms are buckled in published *Michel* unit cells refined to experimental data (Michel et al. 2007, 2010) or derived from ab initio simulation (Pinney et al. 2009). These planes were initially non-buckled in the initial *hybrid* model, but consistently developed buckling during the RMC runs (see arrows in Fig. 8b).

Figure 10 displays bond valence histograms for the Fe sites following RMC optimization. The mean values for the octahedral Fe(1) and Fe(2) sites are 2.92 and 2.70 v.u., respectively, close to the cation charge, with FWHM of 1.4 and 1.2 v.u. These large widths in the bond valence distributions are similar to those reported for RMC refinement of a crystalline oxide, resulting from random RMC moves that are relatively insensitive to bond distortions (Norberg et al. 2009). The incorporation of a bond valence penalty within RMC moves can lead to significantly narrower bond valence range, although we did not incorporate this approach in the present RMC method. We tested whether highly over or under coordinated Fe sites were important for the goodness of fit by removing Fe(1) atoms with bond valence values that did not lie between 2.5–3.5 v.u. Removal of these atoms made a barely perceptible effect on the scattering curves, suggesting that very distorted coordination geometries are an inevitable outcome of the RMC approach. Despite the presence of such sites, the lattice topology may nevertheless be a good representation of the material structure.

The mean bond valence for the tetrahedral site, Fe(3), is 3.4, indicating the trivalent cation to be over bonded by 0.4 v.u on average. In contrast, Michel et al. (2010) and Harrington et al. (2011) found the tetrahedral site to be under bonded by 0.26 and 0.17 v.u., respectively. The bond valence discrepancies thus exceed those for any known stable bulk oxide, emphasizing that the structure depicted in Figure 8 cannot be considered an atomistic model

of an actual ferrihydrite nanoparticle. In our view, however, the bond valence method is not proven to be reliable for assessing the structure of metastable, high-surface-area metal oxide nanomaterials with both structural (i.e., interior) and surface protonation. We sought to use an RMC-derived structure as the starting point for a molecular dynamics simulation. However, these simulation methods require the entire nanoparticle to be correctly protonated and hydrated to fully describe the surface structure (Spagnoli et al. 2009). This is a major outstanding challenge and a topic for ongoing work.

CONCLUDING REMARKS

This study illustrates that whole-nanoparticle RMC modeling can provide insight into the structure of defective nanomaterials that is impossible to obtain from single unit-cell descriptions. Application of this approach to the *Michel* model with partial iron occupancies did not significantly improve agreement with the total scattering data. Our implementation of a single-nanoparticle version of the *Drits* model was also not successful at reproducing the total scattering data. However, creating a lower-symmetry structural model based on a hybrid between the *Drits defect-free* model and the *Michel* model lead to qualitative and quantitative improvement of the match to both X-ray diffraction and PDF data relative to each individual description. However, the RMC-derived structures do not yet satisfy all experimental constraints on composition and structure, indicating the need for additional RMC studies with more powerful computational resources. We draw the following particular conclusions from this study.

First, long-range defect disorder is essential. We attempted to capture a new unit-cell description of ferrihydrite from the best-fit RMC-derived nanoparticle by averaging all displacements of each specific lattice site in the nanoparticle and modifying the location of the equivalent site in the starting unit cell. However, a new 3.6 nm nanoparticle derived from the modified unit cell with random distribution of iron occupancies was not significantly better at predicting the total scattering data than the initial unit cell, emphasizing the importance of structural disorder on the nanometer scale.
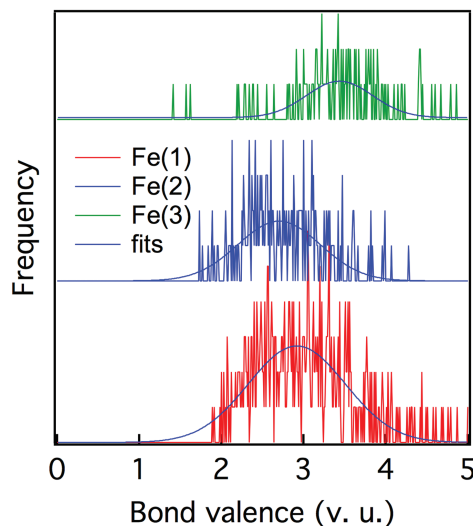
FIGURE 10. Bond valence histograms for the three iron sites, shown with Gaussian fits used to estimate the mean and full-width at half maximum (FWHM) values of the histograms. (Color online.)

Second, near-neighbor structural disorder is essential. In all the RMC runs with the *hybrid* model we observed a strong correlation between the extent of structural disorder and the goodness of the fit to the broad asymmetric peaks in the structure factor (cf. arrow 4 in Fig. 7). Thus, although RMC approaches tend to over estimate structural disorder, we conclude that the presence of considerable disorder in iron-oxygen bond lengths and angles is a genuine aspect of ferrihydrite structure.

Third, RMC models that incorporated tetrahedrally coordinated iron sites consistently obtained better matches to the experimental total scattering data than RMC models in which face-sharing octahedral were incorporated. This finding does not prove the existence of ^{tet}Fe sites because the RMC approach is highly inefficient at finding, through random displacements, suitable changes to local atom positions that would accompany FSO formation. The development of new types of RMC move in which the short-range structural consequences of a localized change (such as site occupation) are more efficiently probed would be a significant advance for the study of defective nanocrystalline materials.

REFERENCES CITED

Barrón, V., Torrent, J., and De Grave, E. (2003) Hydromaghemite, an intermediate in the hydrothermal transformation of 2-line ferrihydrite into hematite. American Mineralogist, 88, 1679–1688.

Bates, S., Zografi, G., Engers, D., Morris, K., Crowley, K., and Newman, A. (2006) Analysis of amorphous and nanocrystalline solids from their X-ray diffraction patterns. Pharmaceutical Research, 23, 2333–2349.

Bedford, N., Dablemont, C., Viau, G., Chupas, P., and Petkov, V. (2007) 3-D structure of nanosized catalysts by high-energy X-ray diffraction and reverse Monte Carlo simulations: Study of Ru. Journal of Physical Chemistry C, 111, 18214–18219.

Bennett, T.D., Goodwin, A.L., Dove, M.T., Keen, D.A., Tucker, M.G., Barney, E.R., Soper, A.K., Bithell, E.G., Tan, J.-C., and Cheetham, A.K. (2010) Structure and properties of an amorphous metal-organic framework. Physical Review Letters, 104, 115503.

Billinge, S.J.L., DiFrancesco, R.G., Kwei, G.H., Neumeier, J.J., and Thompson, J.D. (1996) Direct observation of lattice polaron formation in the local structure of La$_{1-x}$Ca$_x$MnO$_3$. Physical Review Letters, 77, 715–718.

Billinge, S.J.L., and Levin, I. (2007) The problem with determining atomic structure at the nanoscale. Science, 316, 561–565.

Bonneville, S., Van Cappellen, P., and Behrends, T. (2004) Microbial reduction of iron(III) oxyhydroxides: effects of mineral solubility and availability. Chemical Geology, 212, 255–268.

Brese, N.E., and O'Keeffe, M. (1991) Bond-valence parameters for solids. Acta Crystallographica, B47, 192–197.

Brown, I.D., and Altermatt, D. (1985) Bond-valence parameters obtained from a systematic analysis of the inorganic crystal structure database. Acta Crystallographica, B41, 244–247.

Childs, C.W. (1992) Ferrihydrite—a review of structure, properties and occurrence in relation to soils. Zeitschrift für Pflanzenernährung und Bodenkunde, 155, 441–448.

Chupas, P.J., Chapman, K.W., and Lee, P.L. (2007) Applications of an amorphous silicon-based area detector for high-resolution, high-sensitivity and fast time-resolved pair distribution function measurements. Journal of Applied Crystallography, 40, 463–470.

Cismasu, A.C., Michel, F.M., Stebbins, J.F., Levard, C., and Brown, G.E. (2012) Properties of impurity-bearing ferrihydrite I. Effects of Al content and precipitation rate on the structure of 2-line ferrihydrite. Geochimica et Cosmochimica Acta, 92, 275–291.

Cornell, R.M., and Schwertmann, U. (2003) The Iron Oxides: Structure, properties, reactions, occurrences and uses. Wiley VCH, Weinheim.

Cowley, J.M., Janney, D.E., Gerkin, R.C., and Buseck, P.R. (2000) The structure of ferritin cores determined by electron nanodiffraction. Journal of Structural Biology, 131, 210–216.

Dove, M.T., Tucker, M.G., and Keen, D.A. (2002) Neutron total scattering method: simultaneous determination of long-range and short-range order in disordered materials. European Journal of Mineralogy, 14, 331–348.

Drits, V.A., Sakharov, B.A., Salyn, A.L., and Manceau, A. (1993) Structural model for ferrihydrite. Clay Minerals, 28, 185–207.

Dzombak, D.A., and Morel, F.M.M. (1990) Surface Complexation Modeling: Hydrous ferric oxide. Wiley, New York.

Erbs, J.J., Gilbert, B., and Penn, R.L. (2008) Influence of size on reductive dissolution of six-line ferrihydrite. Journal of Physical Chemistry B, 112, 12127–12133.

Farrow, C.L., Juhas, P., Liu, J.W., Bryndin, D., Bozin, E.S., Bloch, J., Proffen, T., and Billinge, S.J.L. (2007) PDFfit2 and PDFgui: computer programs for studying nanostructure in crystals. Journal of Physics-Condensed Matter, 19, 335219.

Fuller, C.C., Davis, J.A., and Waychunas, G.A. (1993) Surface-chemistry of ferrihydrite. 2. Kinetics of arsenate adsorption and coprecipitation. Geochimica et Cosmochimica Acta, 57, 2271–2282.

Gilbert, B., Frandsen, C., Maxey, E., and Sherman, D. (2009) Band-gap measurements of bulk and nanoscale hematite by soft X-ray spectroscopy. Physical Review B, 79, 035108.

Gilbert, B. (2008) Finite size effects on the real-space pair distribution function of nanoparticles. Journal of Applied Crystallography, 41, 554–562.

——— (2009) The crystal chemistry of ferrihydrite. Oral presentation at the M.R.S. Spring Meeting, San Francisco.

Gilbert, B., Huang, F., Zhang, H., Waychunas, G.A., and Banfield, J.F (2004) Nanoparticles: strained and stiff. Science, 305, 651–654.

Goodwin, A.L., Michel, F.M., Phillips, B.L., Keen, D.A., Dove, M.T., and Reeder, R.J. (2010) Nanoporous structure and medium-range order in synthetic amorphous calcium carbonate. Chemistry of Materials, 22, 3197–3205.

Greaves, C. (1983) A powder neutron diffraction investigation of vacancy ordering and covalence in gamma-Fe$_2$O$_3$. Journal of Solid State Chemistry, 49, 325–333.

Guinier, A. (1967) X-ray diffraction in crystals, imperfect crystals and amorphous bodies. W.H. Freeman & Co., San Francisco.

Guyodo, Y, Mostrom, A., Penn, R.L., and Banerjee, S.K. (2003) From nanodots to nanorods: Oriented aggregation and magnetic evolution of nanocrystalline goethite. Geophysical Research Letters, 30, 1512.

Guyodo, Y., Sainctavit, P., Arrio, M.-A., Carvallo, C., Penn, R.L., Erbs, J.J., Forsberg, B.S., Morin, G., Maillot, F., Lagroix, F., Bonville, P., Wilhelm, F., and Rogalev, A. (2012) X-ray magnetic circular dichroism provides strong evidence for tetrahedral iron in ferrihydrite. Geochemistry Geophysics Geosystems, 13, 1–9.

Hammersley, A.P. (1997) FIT2D: An Introduction and Overview, ESRF Internal Report, ESRF97HA02T.

Harrington, R., Hausner, D.B., Xu, W., Bhandari, N., Michel, F.M., Brown, G.E. Jr., Strongin, D.R., and Parise, J.B. (2011) Neutron pair distribution function study of two-line ferrihydrite. Environmental Science & Technology, 45, 9883–9890.

Harrington, R., Neder, R.B., and Parise, J.B. (2012) The nature of X-ray scattering from geo-nanoparticles: Practical considerations of the use of the Debye equation and the pair distribution function for structure analysis. Chemical Geology, 329, 3–9.

Head-Gordon, T., and Hura, G. (2002) Water structure from scattering experiments and simulation. Chemical Reviews, 102, 2652–2670.

Hiemstra, T. (2013) Surface and mineral structure of ferrihydrite. Geochimica et Cosmochimica Acta, 105, 316–325.

Hiemstra, T., and Van Riemsdijk, W.H. (2009) A surface structural model for ferrihydrite I: Sites related to primary charge, molar mass, and mass density. Geochimica et Cosmochimica Acta, 73, 4423–4436.

Hochella, M.F., Kasama, T., Putnis, A., Putnis, C.V., and Moore, J.N. (2005) Environmentally important, poorly crystalline Fe/Mn hydrous oxides: Ferrihydrite and a possibly new vernadite-like mineral from the Clark Fork River Superfund Complex. American Mineralogist, 90, 718–724.

Janney, D.E., Cowley, J.M., and Buseck, P.R. (2001) Structure of synthetic 6-line ferrihydrite by electron nanodiffraction. American Mineralogist, 86, 327–335.

Jansen, E., Kyek, A., Schäfer, W., and Schwertmann, U. (2002) The structure of six-line ferrihydrite. Applied Physics A, 74, S1004–21006.

Jickells, T.D., An, Z.S., Andersen, K.K., Baker, A.R., Bergametti, G., Brooks, N., Cao, J.J., Boyd, P.W., Duce, R.A., Hunter, K.A., and others. (2005) Global iron connections between desert dust, ocean biogeochemistry, and climate.

Science, 308, 67–71.

Jolivet, J.P., Tronc, E., and Chaneac, C. (2006) Iron oxides: From molecular clusters to solid. A nice example of chemical versatility. Comptes Rendus Geoscience, 338, 488–497.

Katz, J.E., Zhang, X., Attenkofer, K., Chapman, K.W., Frandsen, C., Zarzycki, P., Rosso, K.M., Falcone, R.W., Waychunas, G.A., and Gilbert, B. (2012) Electron small polarons and their mobility in iron (oxyhydr)oxide nanoparticles. Science, 337, 1200–1203.

Keen, D.A. (1998) Reverse Monte Carlo refinement of disordered silica phases. In M.F. Thorpe and S.J.L. Billinge, Eds., Local Structure from Diffraction, p. 101–109. Plenum, New York.

——— (2001) A comparison of various commonly used correlation functions for describing total scattering. Journal of Applied Crystallography, 34, 172–177.

Keen, D.A., and McGreevy, R.L. (1990) Structural modelling of glasses using reverse Monte Carlo simulation. Nature, 344, 423–425.

Liu, G., Debnath, S., Paul, K.W., Han, W.Q., Hausner, D.B., Hosein, H.A., Michel, F.M., Parise, J.B., Sparks, D.L., and Strongin, D.R. (2006) Characterization and surface reactivity of ferrihydrite nanoparticles assembled in ferritin. Langmuir, 22, 9313–9321.

Lusvardi, V.S., Barteau, M.A., Chen, J.G., Eng, J. Jr., Frühberger, B., and Teplyakov, A. (1998) An NEXAFS investigation of the reduction and reoxidation of $TiO_2(001)$. Surface Science, 397, 237–250.

Maillot, F., Morin, G., Wang, Y., Bonnin, D., Ildefonse, P., Chaneac, C., and Calas, G. (2011) New insight into the structure of nanocrystalline ferrihydrite: EXAFS evidence for tetrahedrally coordinated iron(III). Geochimica et Cosmochimica Acta, 75, 2708–2720.

Majzlam, J., Grevel, K.-D., and Navrotsky, A. (2003) Thermodynamics of Fe oxides: Part II. Enthalpies of formation and relative stability of goethite (γ-FeOOH), lepidocrocite (γ-FeOOH), and maghemite (γ-Fe_2O_3). American Mineralogist, 88, 855–859.

Manceau, A. (2009) Evaluation of the structural model for ferrihydrite derived from real-space modelling of high-energy X-ray diffraction data. Clay Minerals, 44, 19–34.

——— (2010) PDF analysis of ferrihydrite and the violation of Pauling's Principia. Clay Minerals, 45, 225–228.

——— (2011) Critical evaluation of the revised akdalaite model for ferrihydrite. American Mineralogist, 96, 521–533.

Marchand, P., and Rancourt, D.G. (2009) General model for the aqueous precipitation of rough-surface nanocrystals and application to ferrihydrite genesis. American Mineralogist, 94, 1428–1439.

Masedeh, A.S., Bozin, E.S., Farrow, C.L., Paglia, G., Juhas, P., and Billinge, S.J.L. (2007) Quantitative size-dependent structure and strain determination of CdSe nanoparticles using atomic pair distribution function analysis. Physical Review B, 76, 115413.

Michel, F.M., Barron, V., Torrent, J., Morales, M.P., Serna, C.J., Boily, J.F., Liu, Q.S., Ambrosini, A., Cismasu, A.C., and Brown, G.E. (2010) Ordered ferrimagnetic form of ferrihydrite reveals links among structure, composition, and magnetism. Proceedings of the National Academy of Sciences, 107, 2787–2792.

Michel, F.M., Ehm, L., Antao, S.M., Lee, P.L., Chupas, P.J., Liu, G., Strongin, D.R., Schoonen, M.A.A., Phillips, B.L., and Parise, J.B. (2007) The structure of ferrihydrite, a nanocrystalline material. Science, 316, 1726–1729.

Navrotsky, A., Mazeina, L., and Majzlan, J. (2008) Size-driven structural and thermodynamic complexity in iron oxides. Science, 319, 1635–1638.

Norberg, S.T., Tucker, M.G., and Hull, S. (2009) Bond valence sum: a new soft chemical constraint for RMC profile. Journal of Applied Crystallography, 42, 179–184.

Norberg, S.T., Ahmed, I., Hull, S., Marrocchelli, D., and Madden, P.A. (2009) Local structure and ionic conductivity in the Zr(2)Y(2)O(7)-Y(3)NbO(7) system. Journal of Physics: Condensed Matter, 21, 215401.

Page, K., Hood, T.C., Proffen, T., and Neder, R.B. (2011) Building and refining complete nanoparticle structures with total scattering data. Journal of Applied Crystallography, 44, 327–336.

Paglia, G., Bozin, E.S., and Billinge, S.J.L. (2006) Fine-scale nanostructure in gamma-Al_2O_3. Chemistry of Materials, 18, 3242–3248.

Peak, D., and Regier, T. (2012) Direct observation of tetrahedrally coordinated Fe(III) in ferrihydrite. Environmental Science & Technology, 46, 3163–3168.

Pedersen, H.D., Postma, D., Jakobsen, R., and Larsen, O. (2005) Fast transformation of iron oxyhydroxides by the catalytic action of aqueous Fe(II). Geochimica et Cosmochimica Acta, 69, 3967–3977.

Penn, R.L., Erbs, J.J., and Gulliver, D.M. (2006) Controlled growth of alpha-FeOOH nanorods by exploiting-oriented aggregation. Journal of Crystal Growth, 293, 1–4.

Petkov, V. (1989) RAD, a program for analysis of X-ray diffraction data from amorphous materials for personal computers. Journal of Applied Crystallography, 22, 387–389.

Petkov, V., Zavalij, P.Y., Lutta, S., Whittingham, M.S., Parvanov, V., and Shastri, S. (2004) Structure beyond Bragg: Study of V_2O_5 nanotubes. Physical Review B, 69, 85410.

Pinney, N., Kubicki, J.D., Middlemiss, D.S., Grey, C.P., and Morgan, D. (2009) Density functional theory study of ferrihydrite and related Fe-oxyhydroxides. Chemistry of Materials, 21, 5742–5752.

Prince, K.C., Bondino, F., Zangrando, M., Zacchigna, M., Kuepper, K., Neumann, M., and Parmigiani, F. (2005) Dichroic O 1s photoabsorption and resonant X-ray scattering in haematite (Fe_2O_3). Journal of Electron Spectroscopy and Related Phenomena, 144–147, 719–722.

Proffen, T., and Billinge, S.J.L. (1999) PDFFIT, a program for full profile structural refinement of the atomic pair distribution function. Journal of Applied Crystallography, 32, 572–575.

Proffen, T., and Neder, R.B. (1997) DISCUS: A program for diffuse scattering and defect-structure simulation. Journal of Applied Crystallography, 30, 171–175.

Rancourt, D.G., and Meunier, J.F. (2008) Constraints on structural models of ferrihydrite as a nanocrystalline material. American Mineralogist, 93, 1412–1417.

Rose, J., Manceau, A., Bottero, J.Y., Masion, A., and Garcia, F. (1996) Nucleation and growth mechanism of Fe oxyhydroxide in the presence of PO_4 ions. 1. Fe K-edge EXAFS study. Langmuir, 12, 6701–6707.

Shoemaker, D.P., Li, J., and Seshadri, R. (2009) Unraveling atomic positions in an oxide spinel with two Jahn-Teller Ions: Local structure investigation of $CuMn_2O_4$. Journal of the American Chemical Society, 131, 11450–11457.

Spagnoli, D., Gilbert, B., Waychunas, G.A., and Banfield, J.F. (2009) Prediction of the effects of size and morphology on the structure of water around hematite nanoparticles. Geochimica et Cosmochimica Acta, 73, 4023–4033.

Stumm, W., and Sulzberger, B. (1992) The cycling of iron in natural environments: Considerations based on laboratory studies of heterogeneous redox processes. Geochimica et Cosmochimica Acta, 56, 3233–3257.

Toby, B.H., and Egami, T. (1992) Accuracy of pair distribution function analysis applied to crystalline and non-crystalline materials. Acta Crystallographica, A48, 336–346.

Tronc, E., Belleville, P., Jolivet, J.P., and Livage, J. (1992) Transformation of ferric hydroxide into spinel by Fe(II) adsorption. Langmuir, 8, 313–319.

Tucker, M.G., Dove, M.T., and Keen, D.A. (2001) Application of the reverse Monte Carlo method to crystalline materials. Journal of Applied Crystallography, 34, 630–638.

Tucker, M.G., Goodwin, A., Dove, M.T., Keen, D.A., Wells, S., and Evans, J. (2005) Negative Thermal expansion in ZrW_2O_8: Mechanisms, rigid unit modes, and neutron total scattering. Physical Review Letters, 95, 255501.

van der Zee, C., Roberts, D., Rancourt, D.G., and Slomp, C.P. (2003) Nanogoethite is the dominant reactive oxyhydroxide phase in lake and marine sediments. Geology, 31, 993–996.

Waychunas, G.A., Kim, C.S., and Banfield, J.F. (2005) Nanoparticulate iron oxide minerals in soils and sediments: unique properties and contaminant scavenging mechanisms. Journal of Nanoparticle Research, 7, 409–433.

Wright, A.C. (1988) Neutron and X-ray amorphography. Journal of Non-Crystalline Solids, 106, 1–16.

Xu, W., Hausner, D.B., Harrington, R., Lee, P.L., Strongin, D.R., and Parise, J.B. (2011) Structural water in ferrihydrite and constraints this provides on possible structure models. American Mineralogist, 96, 513–520.

Zhang, H.Z., Chen, B., Banfield, J.F., and Waychunas, G.A. (2008) Atomic structure of nanometer-sized amorphous TiO_2. Physical Review B, 78, 214106.

Zhu, M., Legg, B., Zhang, H., Gilbert, B., Ren, Y., Banfield, J.F., and Waychunas, G.A. (2012) Early stage formation of iron oxyhydroxides during neutralization of simulated acid mine drainage solutions. Environmental Science & Technology, 46, 8140-7.